



Energy Conversion during Asymmetric Magnetic Reconnection

Cong Chang^{1,2,3} , Kai Huang^{1,2,3} , San Lu^{1,2,3} , Rongsheng Wang^{1,2,3} , and Quanming Lu^{1,2,3} ¹ Deep Space Exploration Laboratory/School of Earth and Space Sciences, University of Science and Technology of China, Hefei 230026, People's Republic of China; inhk@ustc.edu.cn² CAS Center for Excellence in Comparative Planetology/CAS Key Lab of Geospace Environment, University of Science and Technology of China, Hefei 230026, People's Republic of China³ Collaborative Innovation Center of Astronautical Science and Technology, Harbin, People's Republic of China

Received 2022 October 20; accepted 2022 December 7; published 2023 January 27

Abstract

Asymmetric magnetic reconnection usually occurs at the Earth's magnetopause, where the magnetic field strength and plasma density are different between the magnetosheath and magnetosphere. In this paper, a two-dimensional particle-in-cell simulation model is used to study the energy conversion during asymmetric magnetic reconnection. Energy conversion can occur in the vicinity of the X-line, magnetosphere separatrix region, and reconnection fronts. In the vicinity of the X-line and magnetosphere separatrix region, the electromagnetic field energy is mainly transferred to electrons, while at the reconnection fronts, the electromagnetic field energy is mainly transferred to ions. For the case with weak magnetic field asymmetry, the reconnection fronts dominate the energy conversion, which is related to the inflowing Poynting flux S_z at the fronts. For the case with strong magnetic field asymmetry, the energy conversion occurs around the X-line and magnetosphere separatrix region, but no longer at the reconnection fronts. This is because the inflowing Poynting flux S_x near the magnetosphere separatrices provides electromagnetic energy for energy conversion. The density asymmetry has no significant effect on the spatial distribution of the energy conversion.

Unified Astronomy Thesaurus concepts: [Plasma physics \(2089\)](#); [Magnetic fields \(994\)](#)

1. Introduction

As an important physical process related to the topological changes of magnetic field lines, magnetic reconnection explosively releases the energy stored in the magnetic field to the plasma, resulting in the acceleration and heating of particles (Parker 1957; Sweet 1958; Yamada et al. 2010; Hesse & Cassak 2020). Energy conversion is one of the fundamental features of magnetic reconnection, which has been widely discussed (Lu et al. 2013; Eastwood et al. 2013; Burch et al. 2016; Wang & Lu 2019; Shu et al. 2021). Satellite observations and kinetic simulations found that energy conversion can occur near the X-line and reconnection fronts (Birn & Hesse 2005, 2010; Angelopoulos et al. 2013; Lu et al. 2013; Goldman et al. 2015; Huang et al. 2015; Khotyaintsev et al. 2017; Zhong et al. 2019; Wang et al. 2020; Yi et al. 2020). The energy is mainly converted to ions at the reconnection fronts, while electrons gain energy mainly near the X-line (Sitnov et al. 2009). It has been found that the energy conversion at the reconnection fronts is stronger than that in the vicinity of the X-line (Goldman et al. 2015; Yi et al. 2019). Recently, Shu et al. (2021) studied the connection between the energy conversion near the X-line and reconnection fronts, and demonstrated that the X-line provides the energy source for the formation of the reconnection fronts, then the fronts gradually dominate the energy conversion in the whole reconnection process.

Most of the previous studies are focused on the symmetric reconnection, where the magnetic field strength and plasma density on both sides of the current sheet are almost the same

(Nagai et al. 2001; Eastwood et al. 2010; Lu et al. 2010; Zhou et al. 2019). However, reconnection in space and astrophysical environments is usually asymmetric, the physical parameters across the reconnecting current sheet can be significantly different (Eriksson et al. 2015; Peng et al. 2017; Wang et al. 2017). A typical example of asymmetric reconnection is magnetopause reconnection at planets' magnetopauses. There have been numerous observations of magnetic reconnection at the Earth's magnetopause, where the magnetic field strength on the magnetosphere side is stronger than that on the magnetosheath side and the plasma density on the magnetosphere side is lower than that on the magnetosheath side (Mozer et al. 2008; Graham et al. 2014; Khotyaintsev et al. 2016; Burch et al. 2016). The characteristics of reconnection rate, electromagnetic fields, and electron and ion flows in asymmetric reconnection are different from those in symmetric reconnection (Cassak & Shay 2007; Mozer et al. 2008; Pritchett 2008; Hesse et al. 2014). Energy conversion and partition in asymmetric reconnection may also differ from that in symmetric reconnection. Satellite observations and numerical simulations have demonstrated that intense energy conversion occurs in the electron diffusion region (EDR) of asymmetric magnetic reconnection (Burch et al. 2016; Genestreti et al. 2017; Cassak et al. 2017; Swisdak et al. 2018; Pritchard et al. 2019; Eastwood et al. 2020), it is a consensus that electrons gain energy in the EDR, which is similar to symmetric reconnection (Wang et al. 2018). However, Song et al. (2019) found that the energy conversion is insignificant at the reconnection front in asymmetric reconnection, and ions do not gain more energy at the front, which is different from symmetric reconnection. In addition, Genestreti et al. (2020) observed obvious energy conversion within the localized pileup of reconnected magnetic flux between the magnetosheath separatrix and the magnetopause. Therefore, it remains



Original content from this work may be used under the terms of the [Creative Commons Attribution 4.0 licence](#). Any further distribution of this work must maintain attribution to the author(s) and the title of the work, journal citation and DOI.

Table 1
The Parameters Used in Cases 1–4

Case	R_B	R_n
1	2	1/3
2	1.5	1/3
3	3	1/3
4	2	1/10

unclear where the energy conversion occurs and how the magnetic energy is partitioned between electrons and ions. In this paper, with two-dimensional (2D) particle-in-cell (PIC) simulations, we investigate the energy conversion during asymmetric magnetic reconnection, and the effects of the amplitude ratio of the magnetic field and the density ratio on both sides of the current sheet on the energy conversion.

2. Simulation Model

We use a 2D PIC simulation code, which has been successfully applied to study symmetric and asymmetric magnetic reconnection (Fu et al. 2006; Huang et al. 2010; Lu et al. 2010; Sang et al. 2018, 2019; Chang et al. 2021). In this model, the initial configuration of electric and magnetic fields is given in the (x, z) plane and updated by solving the Maxwell equations with an explicit leapfrog algorithm. The particle motion is advanced by calculating the Newton–Lorentz equations.

In this model, the initial magnetic field is given as $\mathbf{B}(z) = B_0[\tanh(\frac{z}{\lambda}) + R]\mathbf{e}_x$, where λ is the half width of the current sheet. The strength of magnetic field across the current sheet is controlled by the parameter R , where there is a stronger magnetic field $B_{sp0} = B_0(1 + R)$ on the magnetosphere side and a weaker magnetic field $B_{sh0} = B_0(1 - R)$ on the

magnetosheath side. The amplitude ratio of the magnetic field between the magnetosphere side and the magnetosheath side is $R_B = (1 + R)/(1 - R)$. The initial density of the plasma is $n = n_0[1 - \alpha_1 \tanh(\frac{z}{\lambda}) - \alpha_2 \tanh^2(\frac{z}{\lambda})]$. There is a lower density $n_{sp0} = n_0(1 - \alpha_1 - \alpha_2)$ on the magnetosphere side and a higher density $n_{sh0} = n_0(1 + \alpha_1 - \alpha_2)$ on the magnetosheath side. The density ratio between the magnetosphere side and the magnetosheath side is $R_n = (1 - \alpha_1 - \alpha_2)/(1 + \alpha_1 - \alpha_2)$. The initial temperature ratio of ions and electrons is $T_{i0}/T_{e0} = 4$, where T_{i0} (T_{e0}) is the initial temperature of ions (electrons). The pressure balance condition across the current sheet requires the total pressure $n(T_{i0} + T_{e0}) + B_x^2/2\mu_0$ to be constant, we can get $\alpha_1 = 2R\alpha_2$ and $\alpha_2 = B_0^2/[2\mu_0 n_0(T_{i0} + T_{e0})]$. The simulation calculation domain size is $L_x \times L_z = 80d_i \times 20d_i$ (where $d_i = c/\omega_{pi}$ is the ion inertial length based on the density n_0), and the grid size is $\Delta x = \Delta z = 0.05d_i$. The time step is set to be $\Delta t = 0.001\Omega_i^{-1}$ (where $\Omega_i = eB_0/m_i$ is the ion gyrofrequency). We set $\lambda = 0.5d_i$, $m_i/m_e = 100$ (where m_i denotes ion mass and m_e denotes electron mass), and $c = 15V_A$ (where c denotes the light speed and $V_A = B_0/\sqrt{\mu_0 m_i n_0}$ is the Alfvén speed). In the z -direction, conducting boundary conditions are employed, while periodic boundary conditions are used in the x -direction.

We performed four cases to investigate the effects of the amplitude ratio of the magnetic field R_B and the density ratio R_n on the energy conversion in asymmetric reconnection. The parameters used in the four cases are listed in Table 1.

3. Simulation Results

Figure 1 shows the magnetic field B_z (left) and the energy conversion $J \cdot E$ (right) at $\Omega_i t = 20, 40,$ and 60 for Case 1. At about $\Omega_i t = 20$, there is an obvious enhancement of the reconnected magnetic field B_z near the X-line, and the peak value tends to appear on the high-density magnetosheath side

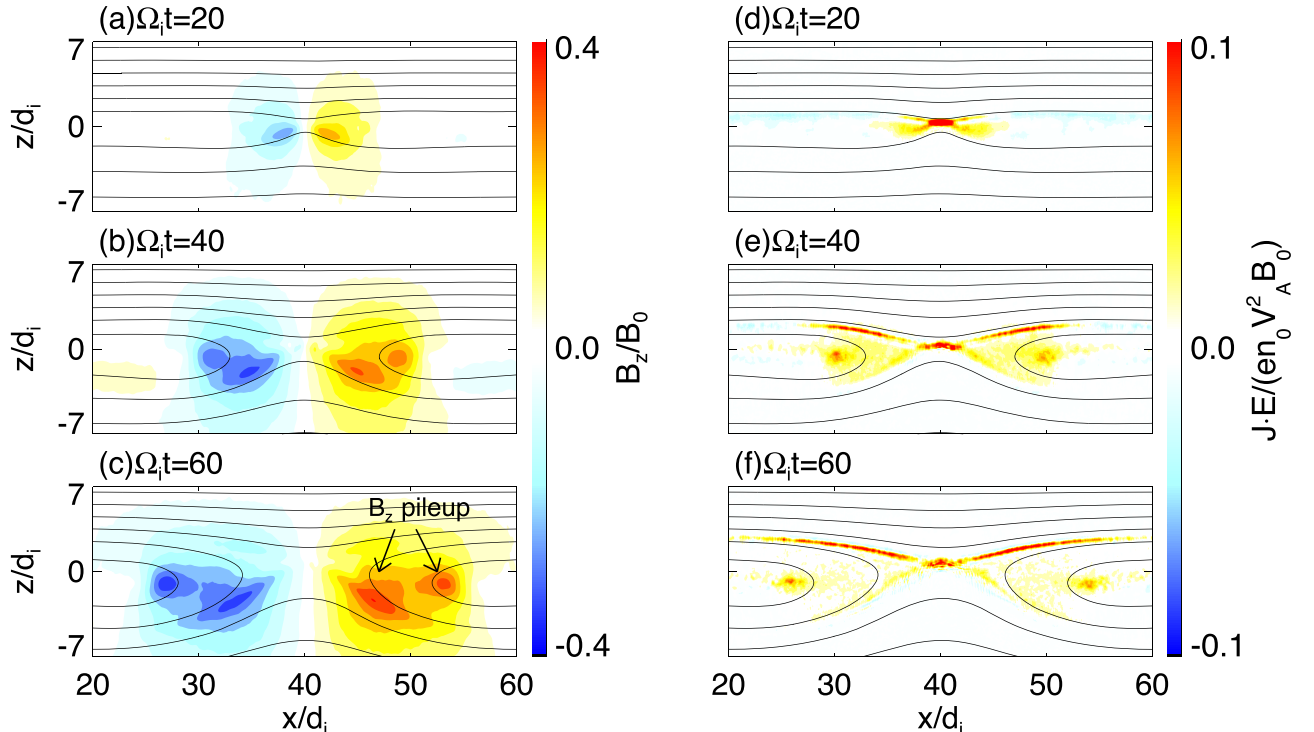


Figure 1. The magnetic field B_z (left) and the energy conversion $J \cdot E$ (right) at $\Omega_i t = 20, 40,$ and 60 for Case 1. The black arrows indicate the two pileup regions of reconnected magnetic B_z , and the black lines represent the in-plane magnetic field.

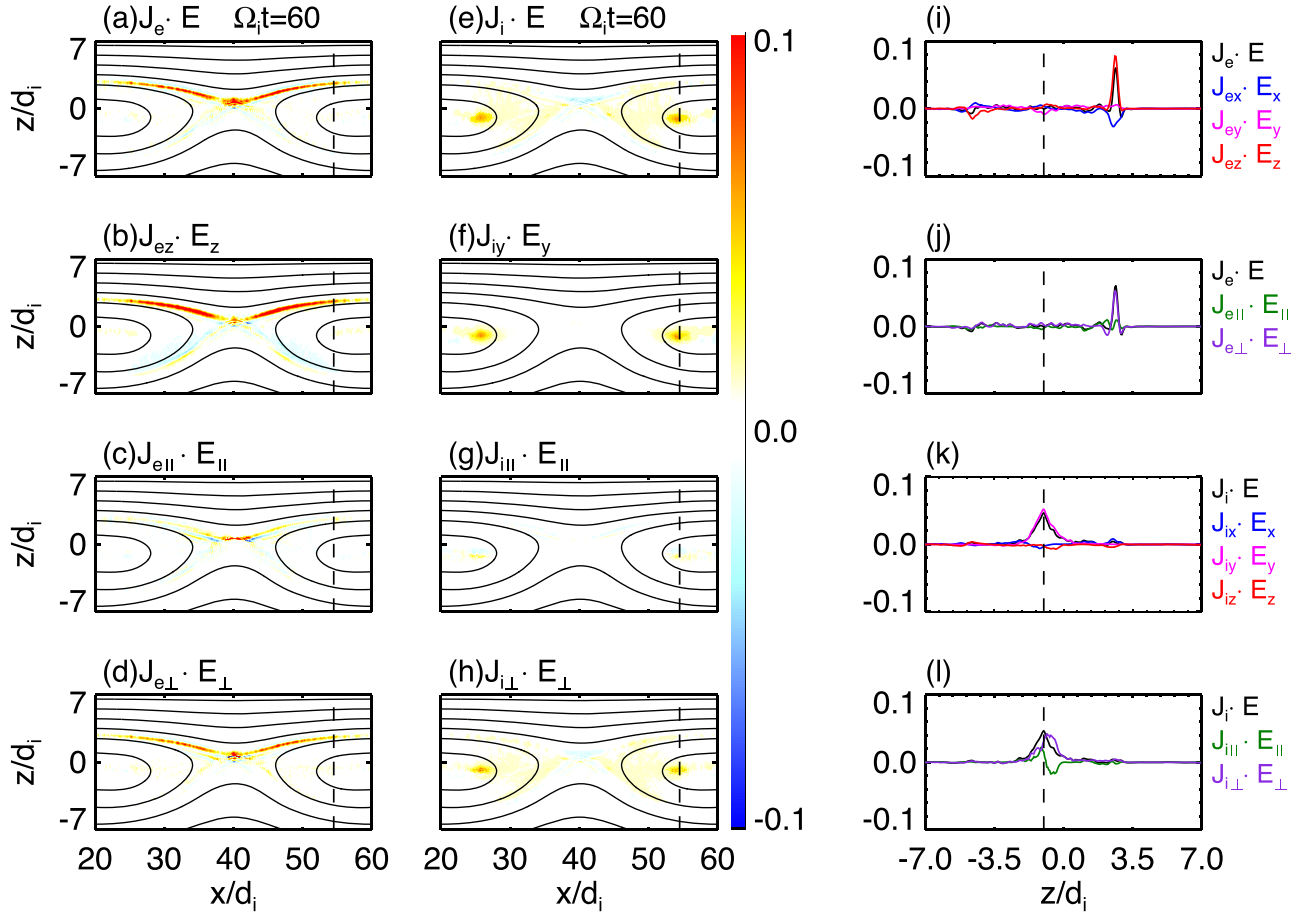


Figure 2. Overview of the energy conversion: (a) $J_e \cdot E$, (b) $J_{ez} \cdot E_z$, (c) $J_{e\parallel} \cdot E_{\parallel}$, (d) $J_{e\perp} \cdot E_{\perp}$, (e) $J_i \cdot E$, (f) $J_{iy} \cdot E_y$, (g) $J_{i\parallel} \cdot E_{\parallel}$, and (h) $J_{i\perp} \cdot E_{\perp}$ at $\Omega_i t = 60$ for Case 1. Panels (i)–(l) show the profiles of $J_e \cdot E$, $J_{ex} \cdot E_x$, $J_{ey} \cdot E_y$, $J_{ez} \cdot E_z$, $J_{e\parallel} \cdot E_{\parallel}$, $J_{e\perp} \cdot E_{\perp}$, $J_i \cdot E$, $J_{ix} \cdot E_x$, $J_{iy} \cdot E_y$, $J_{iz} \cdot E_z$, $J_{i\parallel} \cdot E_{\parallel}$, and $J_{i\perp} \cdot E_{\perp}$ along the vertical dashed lines crossing the reconnection fronts in panels (a)–(h).

(Figure 1(a)). With the development of reconnection, another pair of magnetic field structures with B_z peaks are situated in the outflow region, and then propagate away from the X-line (Figure 1(b)). These structures are similar to the reconnection fronts in previous simulations of magnetic reconnection (Song et al. 2019; Shu et al. 2021). The arrows in Figure 1(c) indicate two pileup regions of B_z , which are the reconnection front and the pileup region near the magnetosheath separatrices. At about $\Omega_i t = 20$, the energy conversion is mainly concentrated in the vicinity of the X-line (Figure 1(d)), that is, the magnetic energy is converted to the plasma ($J \cdot E > 0$). With the development of reconnection and the formation of the reconnection fronts, the energy conversion can also occur at the reconnection fronts and within the narrow channel along the magnetosphere separatrices (Figures 1(e) and (f)). Unlike in symmetric reconnection, the larger energy conversion occurs near the X-line and the magnetosphere separatrices rather than at the reconnection fronts. Previous simulations of symmetric reconnection showed that most of the energy conversion occurs at the fronts and the rest of energy conversion takes place near the X-line and separatrices (Yi et al. 2019; Shu et al. 2021).

Figure 2 shows the detailed analysis of (a)–(d) $J_e \cdot E$ and (e)–(h) $J_i \cdot E$ at $\Omega_i t = 60$ for Case 1. Figures 2(i)–(l) show the profiles of the physical quantities along the vertical dashed lines crossing the reconnection fronts in Figure 2(a)–(h). Figure 2(a) describes the energy conversion to electrons $J_e \cdot E$, and the positive $J_e \cdot E$ is mainly distributed near the X-line and

the magnetosphere separatrices. The primary contribution comes from $J_{ez} \cdot E_z$, as shown in Figures 2(b) and (i). Figures 2(c) and (d) show the parallel and perpendicular components of $J_e \cdot E$, respectively. The parallel component $J_{e\parallel} \cdot E_{\parallel}$ is concentrated near the X-line, and the large $J_{e\perp} \cdot E_{\perp}$ is distributed in the vicinity of the X-line and magnetosphere separatrix region. $J_e \cdot E$ is mainly contributed by $J_{e\perp} \cdot E_{\perp}$ in the magnetosphere separatrix region (Figure 2(j)). Figure 2(e) shows that the positive $J_i \cdot E$ is concentrated at the reconnection fronts, mainly contributed by the $J_{iy} \cdot E_y$ term (Figures 2(f) and (k)). The perpendicular term $J_{i\perp} \cdot E_{\perp}$ is dominant (Figures 2(h) and (l)).

According to Poynting’s theorem (Birn & Hesse 2010) $\frac{\partial}{\partial t} \left(\frac{\epsilon_0 E^2}{2} \right) + \frac{\partial}{\partial t} \left(\frac{B^2}{2\mu_0} \right) + \nabla \cdot \mathbf{S} = -\mathbf{J} \cdot \mathbf{E}$, where $\mathbf{S} = \mathbf{E} \times \mathbf{B} / \mu_0$ is the Poynting vector. Figure 3 shows (a) the energy conversion $\mathbf{J} \cdot \mathbf{E}$ and (b) the divergence of the Poynting flux $\nabla \cdot \mathbf{S}$ at $\Omega_i t = 60$ for Case 1. We find that the amplitude of $\nabla \cdot \mathbf{S}$ is almost equal to $-\mathbf{J} \cdot \mathbf{E}$ near the magnetosphere separatrices and reconnection fronts. In Figures 3(c) and (d), we show the x -component and z -component of the Poynting flux. Different from symmetric reconnection where S_x flows away from the X-line (Lu et al. 2018), in Figure 3(c), the incoming Poynting flux S_x is located below the separatrices on the magnetosphere side, and the outflow of S_x is located above the separatrices. Such a pattern of S_x contributes to the net inward Poynting flux along the magnetosphere separatrices, which provides a source

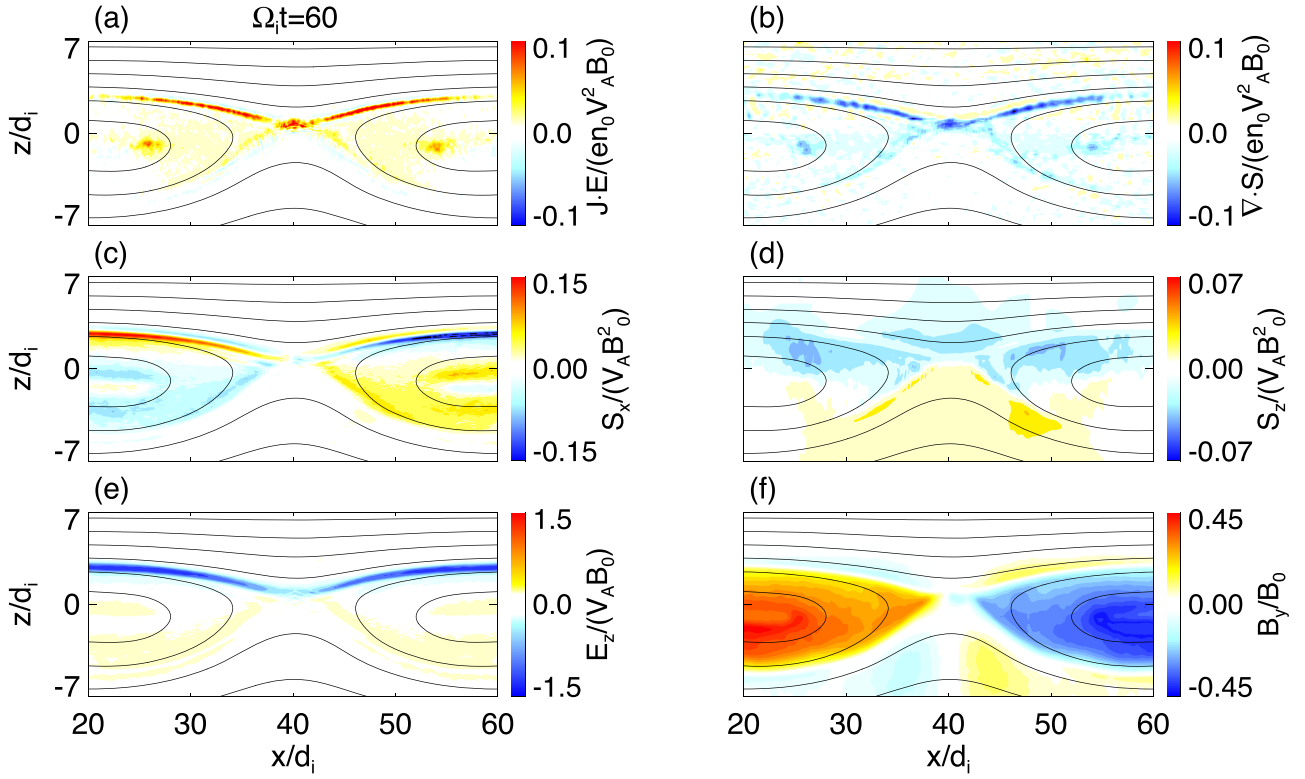


Figure 3. (a) The energy conversion $J \cdot E$, (b) the divergence of the Poynting flux $\nabla \cdot S$, (c) the x -component of the Poynting flux S_x , (d) the z -component of the Poynting flux S_z , (e) the electric field E_z , and (f) the out-of-plane magnetic field B_y at $\Omega_i t = 60$ for Case 1.

of electromagnetic energy for energy conversion. In Figure 3(d), S_z flows into the reconnection fronts, and contributes to the net energy income at the reconnection fronts, which is similar to symmetric reconnection. Then, the electric field E_z and the out-of-plane magnetic field B_y , associated with the Poynting flux S_x are plotted in Figures 3(e) and (f), respectively. The unipolar electric field E_z directed toward the z -direction is distributed along the magnetosphere separatrix, which decelerate the inflowing magnetosheath ions (Pritchett 2008). The out-of-plane magnetic field B_y exhibits a hexapolar pattern. The dominant B_y pattern can cross the center of the current sheet and extend to the magnetosphere side, collocated with strong E_z . Due to $S_x \sim -E_z B_y$, the large E_z and distorted B_y cause the Poynting flux toward the X-line along the magnetosphere separatrices. The two quadrants of B_y originally located on the magnetosphere side only occur in a narrow region, which is related to the outflow of S_x .

The effect of the amplitude ratio of the magnetic field R_B on the energy conversion in asymmetric reconnection is studied by performing Case 2 and Case 3. Figure 4 exhibits (a) the magnetic field B_z , (b) the energy conversion $J \cdot E$, (c) the x -component of Poynting flux S_x , (d) the z -component of Poynting flux S_z , (e) the electric field E_z , and (f) the out-of-plane magnetic field B_y at $\Omega_i t = 33$ for Case 2. In this case, the amplitude ratio of the magnetic field R_B is 1.5. The magnetic field B_z increases on the left and right sides of the X-line, forming a reconnection front that propagates downstream, and there is no significant pileup of B_z near the magnetosheath separatrices. In Figure 4(b), most of the energy conversion $J \cdot E$ occurs at the fronts, contributed by the inflowing Poynting flux S_z (Figure 4(d)), similar to Case 1. $J \cdot E$ distributed near the X-line and magnetosphere separatrices is much weaker, because the pattern of S_x is greatly different to that in Case

1. In Figure 4(c), S_x flows away from the X-line, while the inflowing Poynting flux S_x in Figure 3(c) disappears. In Figures 4(e) and (f), the negative electric field E_z is located in the magnetosphere side. Although the quadrupolar B_y structure is still dominated by the two quadrants in the magnetosheath side, the width of the two quadrants in the magnetosphere side is larger than that in Case 1 (Figure 3(f)). Thus, the Poynting flux S_x associated with E_z and B_y in the magnetosphere side mainly flows out in a narrow region along the magnetosphere separatrices.

Figure 5 plots the same quantities as Figure 4 but at $\Omega_i t = 90$ for Case 3. Increasing R_B to 3, the two pileup regions of B_z are located near the reconnection fronts and magnetosheath separatrices, respectively. The reconnection front slowly moves away from the X-line (Figure 5(a)). The energy conversion decreases, $J \cdot E$ is concentrated in a small region near the X-line, and some perturbations occur in the separatrix region. $J \cdot E$ at the reconnection fronts is negligible (Figure 5(b)). In Figure 5(c), the Poynting flux S_x flows inward along the magnetosphere separatrices, driving the energy conversion in the separatrix region, similar to Case 1. The reversal of S_x on the left and right sides of the X-line (approximately at $x = 42d_i$) causes the divergence of the Poynting flux to occur in a small region near the X-line. In Figure 5(d), the amplitude of S_z is much smaller than that in Case 1 and Case 2, and therefore $J \cdot E$ at the reconnection front is negligible. In Figures 5(e) and (f), the pattern of B_y is similar to that in Case 1; the negative E_z on the magnetosphere side and B_y extending to the magnetosphere side lead to the S_x flows toward the X-line in the separatrix region.

The effect of the density ratio R_n on the energy conversion in asymmetric reconnection is studied by performing Case 4. Other parameters are the same as Case 1, except $R_n = 1/10$.

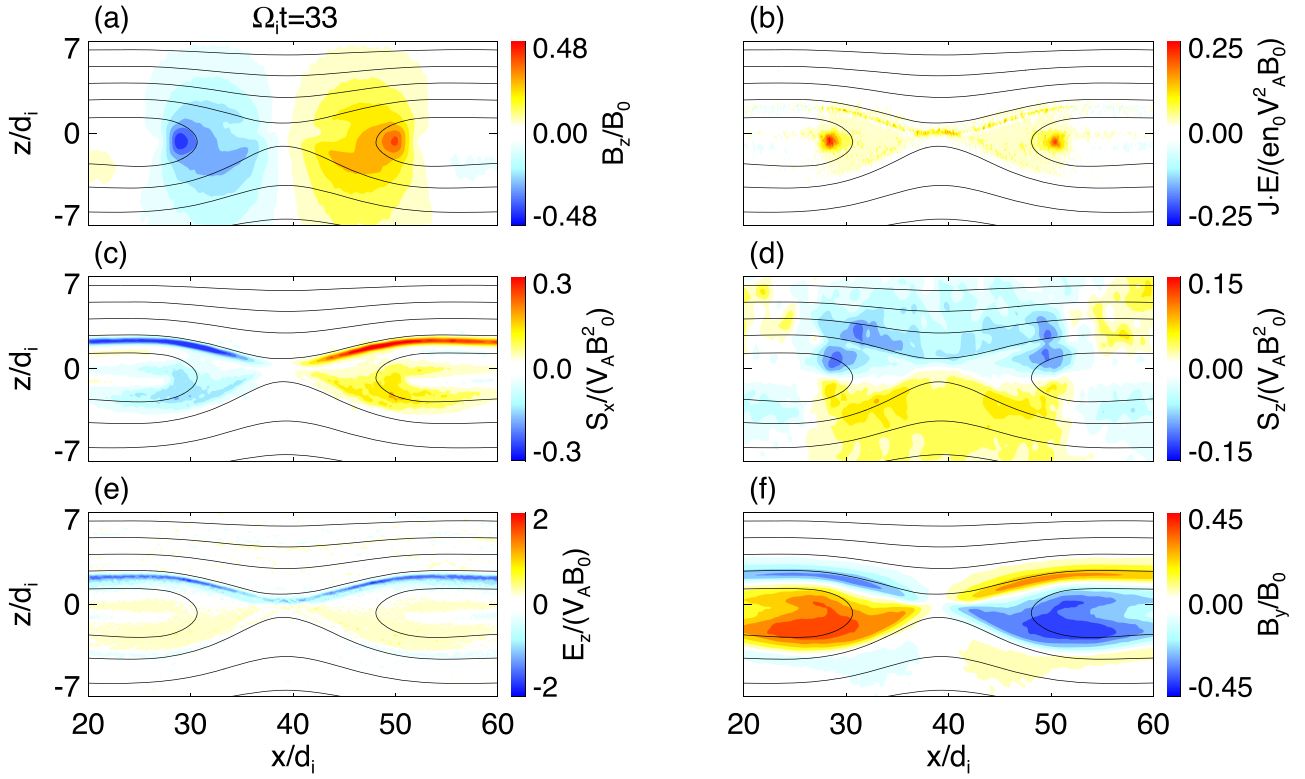


Figure 4. (a) The magnetic field B_z , (b) the energy conversion $J \cdot E$, (c) the x -component of the Poynting flux S_x , (d) the z -component of the Poynting flux S_z , (e) the electric field E_z , and (f) the out-of-plane magnetic field B_y at $\Omega_i t = 33$ for Case 2.

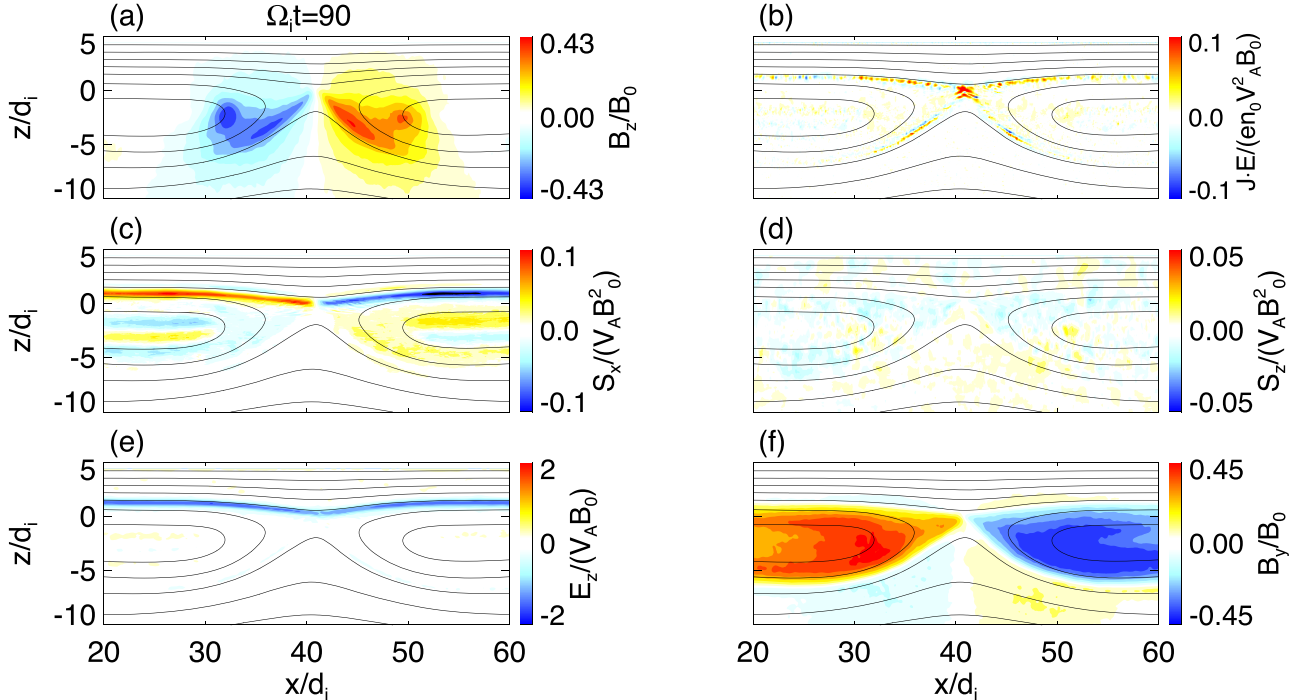


Figure 5. (a) The magnetic field B_z , (b) the energy conversion $J \cdot E$, (c) the x -component of the Poynting flux S_x , (d) the z -component of the Poynting flux S_z , (e) the electric field E_z , and (f) the out-of-plane magnetic field B_y at $\Omega_i t = 90$ for Case 3.

Figure 6 exhibits (a) the magnetic field B_z , (b) the energy conversion $J \cdot E$, (c) the x -component of Poynting flux S_x , and (d) the z -component of Poynting flux S_z at $\Omega_i t = 45$ for Case 4. Similar to Case 1, the pileup of magnetic flux occurs in the outflow region, forming a reconnection front that moves away from the X-line, and another pileup region occurs near the

magnetosheath separatrix. Figure 6(b) shows that most of the energy conversion can occur near the X-line and magnetosphere separatrix, and the remaining energy conversion occurs at the fronts. In the vicinity of the X-line and magnetosphere separatrix, the larger energy conversion is associated with the inflow of S_x , which is controlled by the

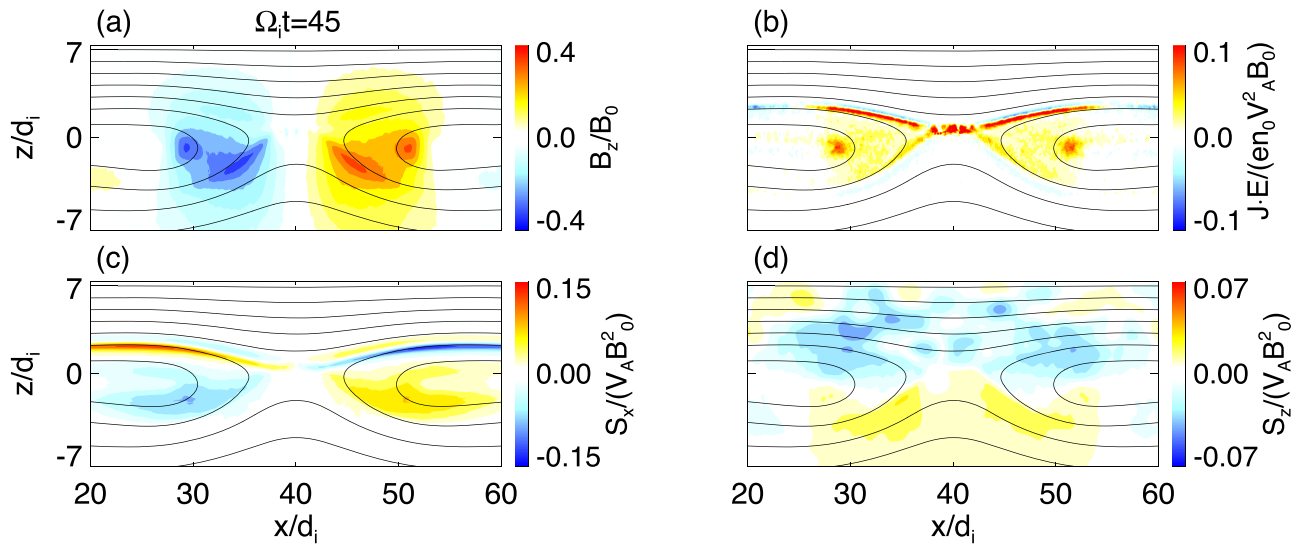


Figure 6. (a) The magnetic field B_z , (b) the energy conversion $J \cdot E$, (c) the x -component of the Poynting flux S_x , and (d) the z -component of the Poynting flux S_z , at $\Omega_i t = 45$ for Case 4.

spatial distribution of the out-of-plane magnetic field (Figure 6(c)). At the fronts, the Poynting flux income is converted to the plasma through $J \cdot E$, and the inflowing Poynting flux is mainly contributed by S_z (Figure 6(d)). Similar results are obtained in Case 1 with $R_n = 1/3$. Therefore, the density ratio does not affect the spatial distribution of energy conversion.

4. Conclusions and Discussion

In this paper, we study energy conversion during asymmetric reconnection using a 2D PIC simulation model. We perform four cases to investigate how $J \cdot E$ is affected by the amplitude ratio of the magnetic field and the density ratio. In asymmetric reconnection, besides the pileup of magnetic flux at reconnection fronts, there is also a magnetic flux pileup region near the magnetosheath separatrices when the amplitude ratio of the magnetic field is large. $J \cdot E > 0$ starts to appear near the X-line, and later also occurs at the reconnection fronts and magnetosphere separatrix region. At the reconnection fronts, the magnetic energy is mainly converted to the ions, and $J_i \cdot E$ is mainly contributed by the ion current J_{iy} and the electric field E_y . $J_i \cdot E$ corresponds to the incoming Poynting flux S_z associated with the reconnection electric field ($\sim -E_y B_x$). In the vicinity of the X-line and magnetosphere separatrix region, the energy conversion is mainly contributed by $J_e \cdot E$, associated with $S_x \sim -E_z B_y$; it is the large $E_z < 0$ and distorted Hall magnetic field B_y that drive the large energy conversion. We find that the energy conversion at the reconnection fronts is stronger than that in other regions for the case with small R_B , which is similar to the symmetric reconnection (Yi et al. 2019; Shu et al. 2021). However, for the case with large R_B , the energy conversion is concentrated around the X-line and magnetosphere separatrices, rather than at the reconnection fronts. With the density ratio R_n decreases, the spatial distribution of energy conversion does not change significantly.

Genestreti et al. (2020) observed intense pileup of reconnected magnetic flux with energy conversion at the magnetosheath separatrix region of the magnetopause reconnection. In our simulations, the energy conversion can also occur within the pileup region near the magnetosheath

separatrices (Figure 5(b)). Although the energy conversion in the magnetosheath separatrix region is much weaker than that in the magnetosphere separatrix region, it is nonnegligible, especially for the case with strong magnetic field asymmetry. By performing PIC simulations, Song et al. (2019) studied the properties of the reconnection fronts in asymmetric reconnection. They stated that the reconnection fronts exist in the outflow region, but the energy conversion at the fronts is insignificant compared with that in the magnetosphere separatrix region. In contrast, our simulation results show that the energy conversion at the fronts is dominated when the amplitude ratio of the magnetic field is not very large (Figure 4(b)). The results in this work, including the spatial distribution of energy conversion in asymmetric reconnection and its dependence on the amplitude ratio of the magnetic field, are expected to be verified by satellite observations in the future.

This work was supported by the National Key Research and Development Program of China, grant No. 2022YFA1604600, the Strategic Priority Research Program of Chinese Academy of Sciences, grant No. XDB 41000000, the NSFC grant 42174181, and the Fundamental Research Funds for the Central Universities WK2080000164, WK3420000017, and KY2080000088. The simulation results described in Section 3 are generated from our computer simulation model. Moreover, the simulation model is described in Section 2.

ORCID iDs

Cong Chang <https://orcid.org/0000-0001-9375-8563>
 Kai Huang <https://orcid.org/0000-0003-3630-309X>
 San Lu <https://orcid.org/0000-0003-2248-5072>
 Rongsheng Wang <https://orcid.org/0000-0002-9511-7660>
 Quanming Lu <https://orcid.org/0000-0003-3041-2682>

References

- Angelopoulos, V., Runov, A., Zhou, X. Z., et al. 2013, *Sci*, 341, 1478
 Birn, J., & Hesse, M. 2005, *AnGeo*, 23, 3365
 Birn, J., & Hesse, M. 2010, *PhPI*, 17, 012109
 Burch, J. L., Torbert, R. B., Phan, T. D., et al. 2016, *Sci*, 352, aaf2939

- Cassak, P. A., Genestreti, K. J., Burch, J. L., et al. 2017, *JGRA*, **122**, 11523
- Cassak, P. A., & Shay, M. A. 2007, *PhPI*, **14**, 102114
- Chang, C., Huang, K., Lu, Q., et al. 2021, *JGRA*, **126**, e29290
- Eastwood, J. P., Goldman, M. V., Phan, T. D., et al. 2020, *PhRvL*, **125**, 265102
- Eastwood, J. P., Phan, T. D., Drake, J. F., et al. 2013, *PhRvL*, **110**, 225001
- Eastwood, J. P., Phan, T. D., Øieroset, M., & Shay, M. A. 2010, *JGRA*, **115**, A08215
- Eriksson, S., Lapenta, G., Newman, D. L., et al. 2015, *ApJ*, **805**, 43
- Fu, X. R., Lu, Q. M., & Wang, S. 2006, *PhPI*, **13**, 012309
- Genestreti, K. J., Burch, J. L., Cassak, P. A., et al. 2017, *JGRA*, **122**, 342
- Genestreti, K. J., Liu, Y. H., Phan, T. D., et al. 2020, *JGRA*, **125**, e27985
- Goldman, M. V., Newman, D. L., & Lapenta, G. 2015, *SSRv*, **199**, 651
- Graham, D. B., Khotyaintsev, Y., Vaivads, A., André, M., & Fazakerley, A. N. 2014, *PhRvL*, **112**, 215004
- Hesse, M., Aunai, N., Sibeck, D., & Bim, J. 2014, *GRL*, **41**, 8673
- Hesse, M., & Cassak, P. A. 2020, *JGRA*, **125**, 25935
- Huang, C., Lu, Q., & Wang, S. 2010, *PhPI*, **17**, 072306
- Huang, S. Y., Fu, H. S., Yuan, Z. G., et al. 2015, *JGRA*, **120**, 4496
- Khotyaintsev, Y., Divin, A., Vaivads, A., Andre, M., & Markidis, S. 2017, *GRL*, **44**, 1234
- Khotyaintsev, Y., Graham, D. B., Norgren, C., et al. 2016, *GRL*, **43**, 5571
- Lu, Q. M., Huang, C., Xie, J. L., et al. 2010, *JGRA*, **115**, A11208
- Lu, S., Lu, Q., Huang, C., & Wang, S. 2013, *PhPI*, **20**, 061203
- Lu, S., Pritchett, P. L., Angelopoulos, V., & Artemyev, A. V. 2018, *PhPI*, **25**, 012905
- Mozer, F. S., Angelopoulos, V., Bonnell, J., Glassmeier, K. H., & McFadden, J. P. 2008, *GRL*, **35**, L17S04
- Nagai, T., Shinohara, I., Fujimoto, M., et al. 2001, *JGR*, **106**, 25929
- Parker, E. N. 1957, *JGR*, **62**, 509
- Peng, F. Z., Fu, H. S., Cao, J. B., et al. 2017, *JGRA*, **122**, 6349
- Pritchard, K. R., Burch, J. L., Fuselier, S. A., et al. 2019, *GRL*, **46**, 274
- Pritchett, P. L. 2008, *JGRA*, **113**, A06210
- Sang, L., Lu, Q., Wang, R., Huang, K., & Wang, S. 2018, *PhPI*, **25**, 062120
- Sang, L., Lu, Q., Wang, R., Huang, K., & Wang, S. 2019, *ApJ*, **877**, 155
- Shu, Y. K., Lu, S., Lu, Q. M., Ding, W. X., & Wang, S. 2021, *JGRA*, **126**, 29712
- Sitnov, M. I., Swisdak, M., & Divin, A. V. 2009, *JGRA*, **114**, A04202
- Song, L., Zhou, M., Yi, Y., Deng, X., & Zhong, Z. 2019, *ApJL*, **881**, L22
- Sweet, P. A. 1958, in *IAU Symp. 6, Electro-magnetic Phenomena in Cosmical Physics*, ed. B. Lehnert (Cambridge: Cambridge Univ. Press), 123
- Swisdak, M., Drake, J. F., Price, L., et al. 2018, *GRL*, **45**, 5260
- Wang, L., Huang, C., Cao, X., Du, A., & Ge, Y. S. 2020, *JGR*, **125**, 28568
- Wang, R. S., Nakamura, R., Lu, Q. M., et al. 2017, *PhRvL*, **118**, 175101
- Wang, S., & Lu, Q. M. 2019, *Collisionless Magnetic Reconnection* (Beijing: Science Press)
- Wang, S., Chen, L. J., Bessho, N., et al. 2018, *JGRA*, **123**, 8185
- Yamada, M., Kulsrud, R., & Ji, H. 2010, *RvMP*, **82**, 603
- Yi, Y., Zhou, M., Song, L., & Deng, X. 2019, *ApJL*, **883**, L22
- Yi, Y., Zhou, M., Song, L., & Deng, X. 2020, *PhPI*, **27**, 122905
- Zhou, M., Deng, X. H., Zhong, Z. H., et al. 2019, *ApJ*, **870**, 34
- Zhong, Z. H., Deng, X. H., Zhou, M., et al. 2019, *GRL*, **46**, 12693